



# Modeling of experimental results for carbon utilization in a carbon fuel cell

Brentan R. Alexander<sup>a,\*</sup>, Reginald E. Mitchell<sup>a</sup>, Turgut M. Gür<sup>b</sup>

<sup>a</sup> Department of Mechanical Engineering, Stanford University, Stanford, CA 94305, USA

<sup>b</sup> Department of Materials Science and Engineering, Stanford University, Stanford, CA 94305, USA

## HIGHLIGHTS

- We model a carbon fuel cell capable of producing electricity from solid fuels.
- The model is validated against experimental data and shows good agreement.
- Results show cells can offer efficiencies of 60% and power densities of 100 mW cm<sup>-2</sup>.
- The model maps the fundamental tradeoff between power density and unit efficiency.

## ARTICLE INFO

### Article history:

Received 20 July 2012

Received in revised form

17 November 2012

Accepted 21 November 2012

Available online 29 November 2012

### Keywords:

Carbon fuel cells

Solid oxide fuel cells

Direct carbon fuel cells

Fuel cells

## ABSTRACT

The carbon fuel cell, a novel electrochemical conversion scheme for the production of efficient electric power from solid carbonaceous fuels, is investigated. A model of the carbon fuel cell is developed, validated, and exercised to explore the interactions between cell geometry, power output, and overall efficiency. The model is built on the Boudouard reaction mechanism and includes experimentally measured kinetic parameters of the electrode and carbon bed reactions. Results indicate that the modeled cell geometry can operate in an optimal regime offering efficiencies near 60% and cell power densities of 100 mW cm<sup>-2</sup>. The model further reveals a fundamental tradeoff between efficiency and power output inherent in a carbon fuel cell, suggesting that high cell efficiencies can be obtained at half of peak power output.

© 2012 Elsevier B.V. All rights reserved.

## 1. Introduction

Finding technologies that can more efficiently transform the chemical energy in carbon-based fuels into electricity is of great importance for mankind in the next century. Any increase in conversion efficiency results in more electricity produced per unit of fuel input, allowing for less reliance on fuels such as coal, a finite resource, or biomass, whose growth requires vast amounts of agricultural land. This also naturally helps to reduce greenhouse gas emissions, which is critically important to mitigating global climate change. Thus, efficient conversion of carbon-based fuels into electricity addresses two of the most important issues facing our planet in the 21st century: sustainable energy production and environmental protection.

Carbon-based fuels, and coal in particular, are vital parts of the electricity generation infrastructure, with coal alone accounting for almost 50% of electricity generated in the United States, and over

40% worldwide [1]. Typically, generation plants convert solid fuels into electricity by burning pulverized coal or biomass in a boiler to heat steam, which then is passed through a turbine. On average, these power plants run at conversion efficiencies of approximately 33% [1]. As environmental regulations are added for sulfur, mercury, and other pollutants, the efficiency of the plant falls as required auxiliary scrubbing equipment is added to the plant.

To further increase conversion efficiencies and allow for distributed electricity production, carbon fuel cell (CFC) devices have been proposed and tested [2–5]. These cells imitate the combustion reaction of carbon, with the exception that the reaction occurs electrochemically and that the reactant and product streams are physically separated by a solid electrolyte membrane and do not mix with each other, allowing for electrical work to be realized from the completion of the overall reaction.

In order for the CFC concept to continue to advance toward commercial applications, a better understanding of the interactions between overall cell efficiency, fuel bed requirements, and maximum electricity production rates are required. This study reports the results of a modeling effort that describes CFC operation dynamics in order to understand the impacts of cell geometry on overall device

\* Corresponding author.

E-mail address: [brentan@stanford.edu](mailto:brentan@stanford.edu) (B.R. Alexander).

performance. The model developed builds upon our earlier models [6,7] that were based primarily on the chemical kinetics of the carbon bed. The present study has greatly expanded the carbon fuel bed model to include the electrochemical kinetics of the fuel cell itself. As a result, the current work represents a complete fuel cell model including both electrochemical and bed kinetics that is capable of describing the carbon fuel cell operational characteristics.

## 2. Solid fuel conversion in a carbon fuel cell

The quest for direct carbon conversion in a fuel cell has been pursued since Becquerel in 1855, and Jacques in 1897 who employed carbon rods as consumable anodes in molten  $K_2NO_3$  and NaOH electrolytes [8,9]. Owing to undesirable side reactions of the electrolyte in these systems, Baur and co-workers later abandoned the molten alkali electrolytes and replaced them by molten salts such as carbonates, silicates and borates [10–12].

In 1937, Baur and Preis suggested that the condition for a chemically stable electrolyte can only be met by the use of an ionically conducting solid electrolyte such as yttria stabilized zirconia (YSZ) [13]. In the 1960's, coal derived gases were employed in high temperature fuel cells [14]. Others pursued utilization of solid fuels inside a molten carbonate electrolyte or molten Sn anode that contains the dispersed carbon particles in an attempt to generate electricity [15–18]. Model studies to achieve the same in molten Ag or Fe anodes have also been published [19,20]. Carbon was also utilized as a consumable anode in fuel cell configurations employing molten hydroxide electrolyte [21]. Recent reports review the progress of carbon fuel cells in more detail using different cell arrangements adopted from various forms of common fuel cell types [22,23].

The process of converting solid carbon in a fluidized bed using a solid oxide fuel cell (SOFC) based arrangement was originally proposed by Gür and Huggins [24]. More recently, Gür, Mitchell and coworkers [2–5] have established in a series of publications the feasibility of generating electricity in a single process step from the conversion of coal and other solid carbonaceous fuels in a specialized carbon fuel cell (CFC) reactor that utilized anode recycle to fluidize the fuel bed and achieve dry gasification.

Recent modeling work has further demonstrated the viability of the solid oxide fuel cells utilizing solid carbon or carbon-derived syngas as a primary fuel source. Liu et al. devised a simplified model of a direct carbon fuel cell utilizing a molten salt in the anode chamber loaded with spherical carbon fuel. By extrapolating on experimentally derived kinetic parameters, the authors verified that smaller fuel particles allowed for increased cell performance, due to an increase in active surface area per unit mass fuel [25]. Another study by Shi et al. examined a one-dimensional solid oxide fuel cell model with a proposed 10-step reaction mechanism for CO oxidation on nickel. The simulations matched well with experimentally derived data [26]. Colpan et al. developed a thermodynamic model of an internal reforming SOFC fueled by bio-syngas and explored the impacts of fuel utilization and exhaust recirculation on overall performance [27].

Recent modeling work from this laboratory have described the detailed chemical reaction kinetics of the carbon fuel bed in a CFC device [6,7]. These works, however, did not include or couple the SOFC electrode kinetics with a model of the carbon bed kinetics, and the results therefore were based upon assumed theoretical current densities that the fuel itself could support without considering rate limitations stemming from the fuel cell electrochemical kinetics.

The carbon fuel cell arrangement modeled in this study is based on this previous work [6] and employs a dense and nonporous solid oxide ceramic electrolyte membrane such as yttria stabilized zirconia (YSZ) that selectively transports oxide ions. The anode

surface is in direct physical contact with the carbon bed, and hence the cell is directly coupled to a Boudouard gasifier within the same chamber. The CFC arrangement, reproduced for clarity in Fig. 1 [6], provides great flexibility in the range of solid fuels that can be utilized in the setup, including different types and grades of biomass and other renewable carbonaceous solids. An additional advantage of this approach is that the use of the YSZ electrolyte membrane excludes the nitrogen in air from entering the process stream, and hence the product effluent is a concentrated stream of  $CO_2$ , which can be readily captured for storage or sequestration.

The overall cell configuration of the CFC can be described as



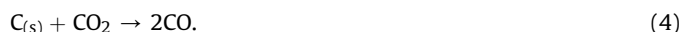
The cathode reaction (denoted by subscript c) is the electrochemical reduction of oxygen by



The primary anode reaction (denoted by subscript a) is the electrochemical oxidation of carbon monoxide by



The carbon monoxide consumed at the anode is generated in the fuel bed within the anode compartment through the Boudouard reaction,



Oxide ions formed during the reduction of oxygen at the cathode migrate through the YSZ electrolyte via lattice vacancies and electrochemically oxidize the CO at the anode. As the oxidation product  $CO_2$  diffuses out from the anode surface, it may react with the nearby carbon in the solid fuel bed, and undergo further gasification through the Boudouard Reaction (4), generating CO, some of which is then oxidized at the anode. This so-called “CO shuttle” mechanism was recently proposed by Gür and Huggins [24] to account for the operating principle of many previous studies using similar cell arrangements [28–32]. Although direct carbon oxidation at the anode surface is theoretically possible, the extremely small total solid–solid interaction area is negligible compared with the gas–surface interaction area. The net reaction for the cell, containing the anode and cathode half-cell reactions as well as the carbon bed gasification reaction, can summarily be written as

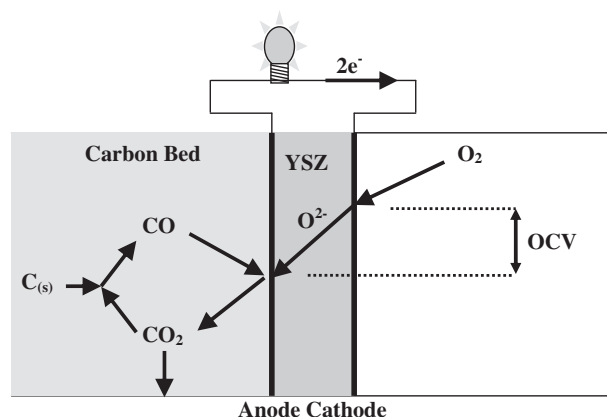


Fig. 1. Schematic of a carbon fuel cell.

Reaction (5) is, in effect, the carbon combustion reaction, however the completion of the reaction in the CFC arrangement leads to four electrons traversing an external circuit for each carbon atom consumed in the bed. The solid carbonaceous fuel in contact with the anode results in a lowering of the oxygen activity, as a portion of the carbon dioxide formed from the electrochemical reactions on the anode surface is reacted to form carbon monoxide via the reverse Boudouard reaction in the bed itself.

The thermodynamic driving force for this cell can be directly calculated from fundamental thermodynamic principles. The concentrations of carbon monoxide and carbon dioxide under Boudouard equilibrium are related by their free energies of formation:

$$\frac{x_{\text{CO}}^2}{x_{\text{CO}_2}} = K_p = e^{-\frac{2\Delta_f G_{\text{CO}} - \Delta_f G_{\text{CO}_2}}{RT}} \quad (6)$$

These equilibrium values for the carbon monoxide and carbon dioxide concentrations can be utilized directly in the Nernst equation, defined as:

$$E_{\text{OCV,air-carbon}} = \frac{\Delta_f G_{\text{CO}_2}^\circ}{-4F} + \frac{RT}{4F} \ln \left( \frac{x_{\text{O}_2}}{x_{\text{CO}_2}} \right), \quad (7)$$

where the concentration of oxygen in the cathode chamber is based upon air. The open circuit potential for this cell, as shown in Fig. 2, hovers around 1 V until approximately 940 K, at which point the OCV increases with temperature. At this temperature of 940 K, the Boudouard reaction equilibrium changes from favoring  $\text{CO}_2$  formation to favoring CO formation. Accordingly, the calculated open circuit voltage changes from following the thermodynamic driving force of a cell reacting carbon and oxygen to form unit activity  $\text{CO}_2$  to one reacting carbon and oxygen to form unit activity CO. This result is shown as two dashed gray lines in Fig. 2. It should be noted that the form of the Nernst equation utilized to calculate the carbon fuel cell OCV is not critical. If a governing cell reaction different than the one used to derive Equation (7) is assumed, and the appropriate Nernst equation developed, the resultant theoretical open circuit voltage will be the same, as the thermodynamic driving force is dependent solely on the free energy difference between the anode and cathode of the cell, which is unchanged regardless of the assumed oxidation mechanism of the carbon in the anode compartment.

### 3. Cell model

To explore the operating space of the CFC and determine the interplay between overall cell efficiency, electricity production rate,

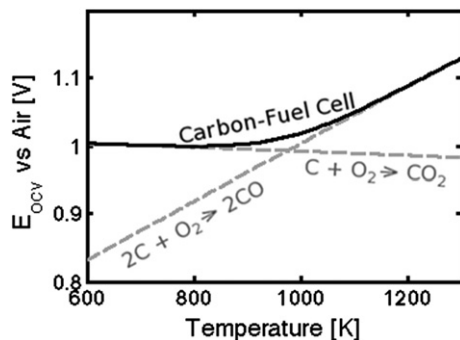


Fig. 2. Thermodynamic open circuit voltages for carbon fuel cell. Dashed lines represent thermodynamic driving forces for theoretical cells with unit product activity.

and bed depth, a model was developed for the combined cell to predict operating parameters under a given set of conditions. The model is based on previous work from our laboratory on the Boudouard reaction mechanism and kinetic parameters for an activated carbon fuel, which is used in this study [2].

To model the global gasification reaction (Reaction (5)) occurring in the fuel bed, the Boudouard mechanism put forth by Ma is used [33]. Previous work in our lab has shown this mechanism to be effective in modeling Boudouard gasification kinetics. This mechanism is listed in Table 1 and is made up of five elementary reactions, two of which can also occur in reverse. In the table,  $C_f$  represents a free surface carbon site,  $C(k)$  is a carbon site with species  $k$  adsorbed on the surface, and  $C_b$  represents a carbon atom in the bulk of the material. Reaction 1f and Reaction 2, which govern the adsorption of oxygen onto the carbon surface and the reaction of adsorbed oxygen to form CO, respectively, are the rate limited and most important reactions in this mechanism. The Arrhenius form was assumed for each elementary reaction, yielding a set of kinetic parameters consisting of seven pre-exponential terms,  $A$ , and seven activation energies,  $E$ , that completely describe the mechanism for any given carbonaceous fuel.

The activated carbon fuel used in the experimental setup is used in this model, and its kinetic parameters were previously found through a series of experiments in a thermogravimetric analyzer (TGA) facility [2]. Char samples of known mass were loaded into the TGA and reacted to completion over a range of temperatures from 800 °C to 1000 °C. The gaseous environment was also varied from test to test, with various mixtures of CO,  $\text{CO}_2$ , and  $\text{N}_2$  used for different runs. The sample mass was measured as a function of time during conversion, and the normalized rate of mass loss, the reactivity, was determined for each case as a function of particle conversion. The kinetic parameters of reactions 2 and 4r were determined directly through temperature programmed desorption (TPD) measurements for loading atmospheres of CO and  $\text{CO}_2$ . The theoretical development of Brunauer, Emmett and Teller (BET), which applies Langmuir adsorption theory to multiple layers of gas phase adsorbing species onto an active surface, was used to determine the specific surface area of the char [34,35]. The  $\text{CO}_2$  partial pressure in the environment surrounding a char sample was adjusted in step intervals over time, and the mass changes of the char particles were measured. Multiple BET measurements were performed at different extents of char conversion, yielding both an initial specific surface area,  $S_{g,C,0}$ , and a structural parameter,  $\psi$ , that can be used to predict the specific surface area,  $S_{g,C}$ , as a function of char conversion according to the function derived from the results of Bhatia and Perlmutter [36]

$$S_{g,C} = S_{g,C,0} \sqrt{1 - \psi \ln(1 - x_C)}, \quad (8)$$

where  $x_C$  is the char extent of conversion, defined as

$$x_C = 1 - \frac{m_C(t)}{m_{C,0}}, \quad (9)$$

Table 1  
Boudouard reaction mechanism [33].

Reaction
1f: $C_f + \text{CO}_2 \rightarrow C(\text{O}) + \text{CO}$
1r: $C(\text{O}) + \text{CO} \rightarrow C_f + \text{CO}_2$
2: $C_b + C(\text{O}) \rightarrow \text{CO} + C_f$
3: $C_b + C(\text{O}) + \text{CO}_2 \rightarrow 2 \text{CO} + C(\text{O})$
4f: $C_f + \text{CO} \rightarrow C(\text{CO})$
4r: $C(\text{CO}) \rightarrow C_f + \text{CO}$
5: $\text{CO} + C(\text{CO}) \rightarrow \text{CO}_2 + 2 C_f$

The remaining kinetic parameters were found by fitting the reaction mechanism to the TGA datasets.

These kinetic parameters were utilized in a two-dimensional axisymmetric finite element model of the carbon char bed. The bed is divided into a sufficient number of interconnected differential volume elements in which the carbon particles are uniformly dispersed. The carbon particles are assumed fixed and confined to the volume elements, while gaseous species flow by convective and diffusive processes throughout the bed. The gas phase mass conservation in the bed, coupled with Darcy's Law, gives

$$\nabla \cdot (\rho \vec{u}) = S_g C_{V_{\text{free}}} \frac{m_c}{V_{\text{free}}} \left( \hat{M}_{\text{CO}} \hat{R}_{\text{CO}} + \hat{M}_{\text{CO}_2} \hat{R}_{\text{CO}_2} \right), \quad (10)$$

$$\vec{u} = -\frac{\kappa}{\mu} \nabla p, \quad (11)$$

where  $\kappa$  can be estimated using the Blake-Kozeny equation [36],  $V_{\text{free}}$  is defined as the total reactor volume minus the volume occupied by carbon particles, and  $\hat{R}_{\text{CO}}$  and  $\hat{R}_{\text{CO}_2}$  are calculated using the local CO and CO<sub>2</sub> concentrations and the reaction mechanism shown in Table 1.

Gas transport through the bed is described for both CO and CO<sub>2</sub> by using the species conservation equation

$$\nabla \cdot \left( -D_{\text{eff}} \nabla C_k + C_k \vec{u} \right) = S_g C_{V_{\text{free}}} \frac{m_c}{V_{\text{free}}} \hat{R}_i, \quad (12)$$

where  $D_{\text{eff}}$  is calculated based on the Chapman-Enskog binary diffusivity of CO and CO<sub>2</sub>, bed porosity, and bed tortuosity, assuming ideal gas behaviors [37].

The domain of this problem is assumed to be based on a button cell configuration, and is taken as a cylinder with radius  $r_o$ , equal to the inner radius of the anode chamber, and height,  $h$ , equal to the depth of the particle bed, as shown in Fig. 3. The boundary condition at the top of the bed ( $z = h$ ), is modeled as an open surface where any mass flux out of the system is due to convection. The anode surface ( $z = 0$ ) is modeled as a specified flux condition corresponding to a current density distribution  $i$ . The oxygen ion flux,  $j_o$ , into the system is related to  $i$  by  $j_o = i/(2F)$  where  $F$  is Faraday's constant. A convective flux exists at the anode boundary due to the oxidation of CO to CO<sub>2</sub>, and this Stefan velocity,  $\vec{u}(r, 0)$  is given by

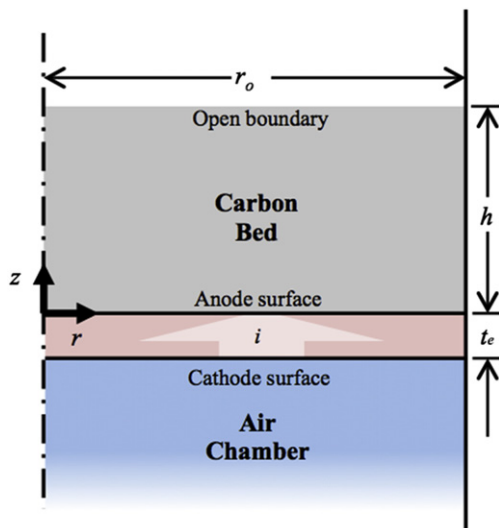


Fig. 3. Schematic of the CFC domain modeled.

$$\vec{u}(r, 0) = \left( \frac{i(r)}{2F} \right) \left( \frac{\hat{M}_{\text{CO}_2} - \hat{M}_{\text{CO}}}{\rho} \right) \hat{z}, \quad (13)$$

The current density distribution  $i(r)$  at the anode surface was found by calculating the current density distribution that produced a given voltage for the cell. This voltage,  $E$ , was an input to the model and is related to the various loss mechanisms in the cell by the relation

$$E = E_{\text{OCV}} - n_{\text{electrolyte}} - n_{\text{anode}} - n_{\text{cathode}}, \quad (14)$$

where  $E_{\text{OCV}}$  is the open circuit voltage of the cell at the reactant concentrations solved for at the electrode surfaces,  $n_{\text{electrolyte}}$  is the voltage loss from ion conduction through the YSZ electrolyte, and  $n_{\text{anode}}$  and  $n_{\text{cathode}}$  are the activation losses from the anode and cathode, respectively.  $E_{\text{OCV}}$  is directly calculated for each cell using Equations (6) and (7), where the concentrations of the gas species at the electrode surfaces are calculated directly from the model itself. This means that mass transport losses are included in this term and do not need to be added separately.

The cell voltage loss for the cell from oxygen ion conduction through the electrolyte,  $n_{\text{electrolyte}}$ , is calculated based on Ohm's law

$$n_{\text{electrolyte}} = i \frac{t_e}{\sigma}, \quad (15)$$

where  $\sigma$  is the ionic conductivity of YSZ at temperature  $T$  and is found from published values.

The activation overpotentials at the anode and cathode,  $n_{\text{anode}}$  and  $n_{\text{cathode}}$ , are calculated using a Butler-Volmer model of electrode kinetics. The local current density is related to the overpotential for an electrode through the relation

$$i = i_0 \left\{ e^{\frac{\alpha_{\text{eff}} i}{RT}} - e^{(\alpha-1) \frac{i}{RT}} \right\}. \quad (16)$$

In the cathode chamber, gas phase convection and diffusion velocity vectors are found by solving the Navier-Stokes equations along with the diffusion equation

$$\rho \frac{D\vec{v}}{Dt} = -\nabla p + \mu \nabla^2 \vec{v}, \quad (17)$$

$$\frac{\partial \rho}{\partial t} + \rho (\nabla \cdot \vec{v}) = 0, \quad (18)$$

$$J_k = -D \nabla C_k, \quad (19)$$

A binary mixture of oxygen and nitrogen is assumed. At the cathode surface, a Stefan flux exists due to the reduction of oxygen, and this boundary condition is represented as

$$\vec{u}(r, -t_e) = -\left( \frac{i}{4F} \right) \left( \frac{-\hat{M}_{\text{O}_2}}{\rho} \right) \hat{z}, \quad (20)$$

The model is implemented in Matlab, and uses COMSOL, a multiphysics finite element software package, to solve the equations. Due to the highly coupled aspect of the problem, the solution is arrived through a nonlinear iterative solver with linearized solutions found at each step using the PARDISO sparse solver. It is useful to consider a simplified solution process to gain insight into the workings of the numerical model. If we consider a cell model based on the domain defined in Fig. 3, the coupled nature of the solution becomes apparent: the cell voltage,  $E_{\text{OCV}}$ , is dependent



upon the local concentrations of reactant and product species, as defined in Equation (7). These local gas concentrations, however, depend upon the flux of oxygen ions into and out of each chamber through the electrolyte, which is an analog to the current density  $i(r)$  in the cell. This current density, in turn, is calculated using Equations (14)–(16). These equations, however, depend on our original unknown: the open circuit voltage  $E_{OCV}$ .

To overcome this coupling, a starting guess is given for the current density distribution  $i(r)$  in the cell. This guess is based upon experimental  $I$ – $V$  data and attempts to give the model a starting point near the eventual solution. Poor initial guesses can lead the model to find local maximum points or non-physical solutions. This initial guess is used to solve for the gas phase concentrations throughout the entire system. These concentrations can then be utilized to calculate the cell open circuit voltage,  $E_{OCV}$ , and the cell current density distribution  $i(r)$  at the voltage of interest  $E$  is calculated from this value. This represents the start of the next iteration step. The new solution value for  $i(r)$  is compared against the guess, and if these values match, the model has converged to a final valid solution. If the values differ, however, the new solution value of  $i(r)$  is used as a new guess and the process is repeated until convergence is achieved.

The model utilizes a quasi-steady assumption, since the time scale for the gases in the bed to equilibrate into a steady condition is short compared to the time scale for char burnout. As a result, the dependence of the char bed physical parameters as a function of char conversion and therefore time, which directly impact the rate of char conversion in the bed, is not solved for by the model, but is instead fed into the model as an input by setting the char conversion parameter  $x_c$ . The conversion parameter is then used to directly calculate the bed physical parameters at any point in time through Equations (8) and (9). The model therefore solves for the steady state conditions for a given set of parameters, which are set based upon the model input  $x_c$ .

To calculate the mass flows in the anode chamber, the mixed-mean mole fractions of CO and CO<sub>2</sub> exiting the bed,  $X_{CO,r=r_0}$  and  $X_{CO_2,r=r_0}$  respectively, are determined for each case. The flow of carbon out of the system in the form of its oxides, which is the same as the makeup flow of solid carbon required to feed the fuel bed, can then be directly found and converted into the mass flow of makeup char into the system by

$$\dot{m}_{char} = \left( \frac{\hat{M}_C}{Y_{C, char}} \right) \left( \frac{X_{CO, z=h} + X_{CO_2, z=h}}{X_{CO, z=h} + 2X_{CO_2, z=h}} \right) \int_0^{r_0} \frac{i}{F} \pi r dr, \quad (21)$$

Similarly, the outlet mass flows for carbon monoxide and carbon dioxide can be readily calculated as

$$\dot{m}_{CO} = \hat{M}_{CO} \left( \frac{X_{CO, z=h}}{X_{CO, z=h} + 2X_{CO_2, z=h}} \right) \int_0^{r_0} \frac{i}{F} \pi r dr, \quad (22)$$

$$\dot{m}_{CO_2} = \hat{M}_{CO_2} \left( \frac{X_{CO_2, z=h}}{X_{CO, z=h} + 2X_{CO_2, z=h}} \right) \int_0^{r_0} \frac{i}{F} \pi r dr, \quad (23)$$

The oxygen mass flow into the system can be expressed as

$$\dot{m}_{O_2} = \hat{M}_{O_2} \int_0^{r_0} \frac{i}{2F} \pi r dr \quad (24)$$

An overall cell mass balance can then be performed to ensure model consistency. The various model parameters used in this

model to predict bed performance, including the kinetic and fuel parameters for activated carbon, are listed in Table 2.

#### 4. Overall cell efficiency

In addition to the electrical power produced, the overall efficiency of the cell is an important parameter to calculate. Traditional definition of electrochemical efficiency, described as the product of the voltage efficiency, coulombic efficiency, and fuel utilization, for fuel cells typically employing gaseous (or liquid) fuels where the fuel activity or concentration monotonically decreases along the electrode surface as reaction proceeds are insufficient to fully describe the complexities of the CFC system where the solid carbon activity is always unity until all solid fuel is consumed entirely.

The important differentiator from a traditional cell is that solid fuel is used in the CFC device, and all the solid carbon that is fed into the cell is oxidized in some form when it leaves the cell. In a traditional efficiency definition, this would equate with a fuel utilization term of 100%. However, the extent to which each carbon atom is oxidized when it leaves the cell is important in overall cell efficiency. Carbon that leaves the cell in the form of carbon monoxide is only partially oxidized, and as a result only two electrons traverse the external circuit for each carbon atom converted to CO. Carbon that leaves the cell as carbon dioxide, however, has been fully oxidized and four electrons traverse the external circuits for each carbon utilized. As a result, the oxidation state of the carbon leaving the system is an important parameter in overall cell efficiency, and must also be included in any useful efficiency calculation.

To overcome these issues, overall cell efficiency for the CFC system is defined based on a an energy balance of the fuel cell system as

$$\eta_{cell} = \frac{P_{out}}{\dot{m}_{char} HHV_{char}}, \quad (25)$$

where  $P_{out}$  is the total power of any produced electricity. This relation for cell efficiency is useful because it overcomes the shortcomings of the traditional electrochemical cell efficiency definition highlighted above. The numerator of the efficiency term includes the electric power produced and the denominator is made up of a term for the fuel requirement, represented by its higher heating value. We can consider two identical CFC devices, with the

**Table 2**  
Parameters used in CFC model [2].

Parameter	Value	Units
$A_{1f}$	$5.0 \times 10^3$	$\text{kJ mol}^{-1}$
$E_{1f}$	$1.84 \times 10^2$	
$A_{1r}$	$1.08 \times 10^2$	$\text{kJ mol}^{-1}$
$E_{1r}$	$8.97 \times 10^2$	
$A_2$	$1 \times 10^{13}$	$\text{kJ mol}^{-1}$
$E_2$	$3.75 \times 10^2$	
$A_3$	$1 \times 10^{-4}$	$\text{kJ mol}^{-1}$
$E_3$	$5.8 \times 10^1$	
$A_{4f}$	$8.77 \times 10^{-1}$	$\text{kJ mol}^{-1}$
$E_{4f}$	$1.48 \times 10^2$	
$A_{4r}$	$1 \times 10^{13}$	$\text{kJ mol}^{-1}$
$E_{4r}$	$4.55 \times 10^2$	
$A_5$	$1.0 \times 10^7$	$\text{kJ mol}^{-1}$
$E_5$	$2.62 \times 10^2$	
$S_{gC,0}$	$7.50 \times 10^5$	$\text{m}^2 \text{kg}^{-1}$
$\rho_{bulk}$	$8.038 \times 10^2$	$\text{kg m}^{-3}$
$\psi$	3.0	–
$HHV_{char}$	$2.687 \times 10^4$	$\text{kJ kg}^{-1}$
$Y_{C, char}$	75.89	% Mass
$\sigma_{YSZ}$	10	$\text{S m}^{-1}$

exception that one cell has a fuel bed height larger than the other, and with the requirement that the bed heights in both cells are sufficiently large as to not materially change the electrochemical conditions of the cells. If both of these cells are operated at the same current and voltage conditions, then the numerator in the efficiency definition in Equation (25) will be the same for both cells. For the cell with the larger bed height, however, the increased residence time of  $\text{CO}_2$  molecules percolating through the bed from the anode toward the exit will result in more of the molecules reacting with the fuel in the bed via the Boudouard reaction and forming CO. The end result will be an anode effluent with a higher concentration of CO than in the cell with the shorter bed, and therefore with a larger makeup char mass flow rate,  $\dot{m}_{\text{char}}$ . This scenario demonstrates that the cells, despite operating at identical conditions, will have different efficiencies due to the different overall mean oxidation state of carbon exiting the system.

## 5. Experimentation and verification

In order to verify the veracity of the model and find values for necessary model inputs, a planar cell was constructed and investigated. The cell was constructed in a button cell geometry using a YSZ electrolyte ceramic disk (1 cm diameter and 0.1 mm thick, MarkeTech International). A nickel cermet electrode was screen-printed onto the anode surface of the cell and a powder of LSM-YSZ composite (NexTech Materials) was used to form the cathode electrode. The cell was affixed to the end of a YSZ tube using an albite glass seal. The active area of the electrodes after this process was approximately  $0.18 \text{ cm}^2$ . Platinum mesh current collectors were placed in contact with each electrode, and a thermocouple was affixed 1 cm from the anode surface to monitor overall temperature.

Approximately 1 g of activated carbon (Fisher Scientific) char was fed into the anode chamber to a depth of 1 cm, and a small helium purge flow was introduced to the top of the chamber to reduce oxygen infusion from the environment. The cell was placed into a quartz reactor vessel and lowered into a cylindrical heater. Dried air was fed into the cathode chamber. A schematic of the experimental setup is shown in Fig. 4.

The cell was interrogated over a range of temperatures from 700 to  $1000^\circ\text{C}$  using a PAR 173 potentiostat/galvanostat and a Solartron 1250 frequency response analyzer. The current–voltage ( $I$ – $V$ ) response was measured for the cell at each experimental temperature. Electrochemical impedance spectra (EIS) were also taken at multiple offset voltages. For each temperature tested in the cells, between 6 and 8 EIS tests were conducted, all with a 20 mV signal amplitude and a range of frequencies from 0.5 Hz to 65 kHz, at an

interval of 12 measurements per decade. Gas chromatography of both anode and cathode outlet gases was performed at the completion of each spectroscopy measurement in order to verify both the physical integrity of the cell and the transfer of oxygen from the cathode to the anode stream.

The measured  $I$ – $V$  responses and the calculated power curves of the test cell over a range of temperatures are shown in Fig. 5. The cell OCV was measured to range between 0.9 and 1 V, slightly below the thermodynamically predicted value. Short circuit current for the cell increased with operating temperature, as expected, and reached a peak value of just under  $800 \text{ mA cm}^{-2}$  when the cell was operating at  $1000^\circ\text{C}$ . At this same temperature, the cell exhibited a peak power density of  $143 \text{ mW cm}^{-2}$  at 0.46 V.

The test results indicate that the cell is capable of operating at practical current densities approaching  $300 \text{ mA cm}^{-2}$  and moderate power densities upwards of  $140 \text{ mW cm}^{-2}$ . The slight drop in OCV from the thermodynamically expected value can be explained by the presence of the helium purge flow in the anode chamber, and its removal would yield a slight increase in overall performance. The non-optimized nature of the devices also points to further improvements in cell performance by producing optimized cells in a more controlled and reproducible production environment.

EIS measurements were also taken, and three representative EIS spectra for the cell at  $900^\circ\text{C}$  are shown in Fig. 6. The spectra reveal an electrolyte resistance of approximately  $1 \Omega$  in good agreement with the expected value based upon published YSZ conductivity measurements. In addition, two semi-circular lobes are clearly evident in the spectrum, corresponding to the activation losses of each electrode surface.

In order to better understand the observed spectra and extract useful information on electrode processes from the data, an equivalent circuit model of the cell operation was developed to describe and fit the experimentally measured impedance spectra using ZPlot (Scribner Associates). The model consists of a single resistor in series with two network blocks, each consisting of a single resistor element and a constant phase element in parallel with each other. The proposed equivalent circuit model is shown schematically in Fig. 7.

The first resistor, labeled  $R_e$  in Fig. 7, represents the ohmic resistance of the cell and experimental setup. Each parallel circuit block represents the combined resistive and capacitive behavior of each electrode reaction process. The resistor, labeled  $R_a$  and  $R_c$  for the anode and cathode respectively, models the activation loss that occurs at the electrode interface. The constant phase element is in nature a capacitive element that accounts for the non-ideal capacitive behavior of the electrode interface.

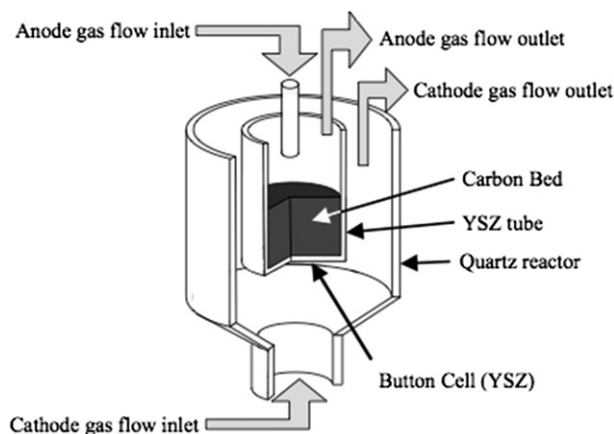


Fig. 4. Schematic of button cell experimental setup.

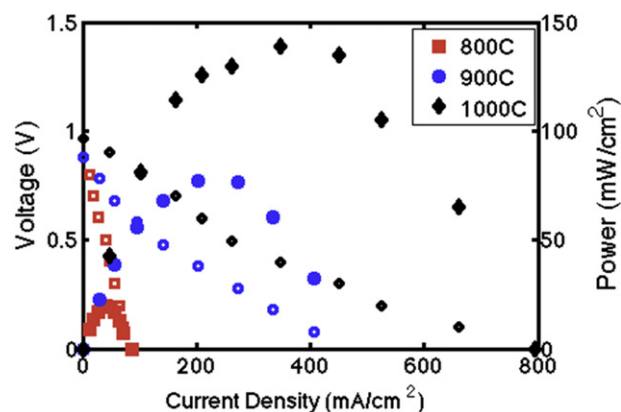


Fig. 5. The DC current–voltage (open) and current–power (closed) response of the test cell over a range of temperatures.

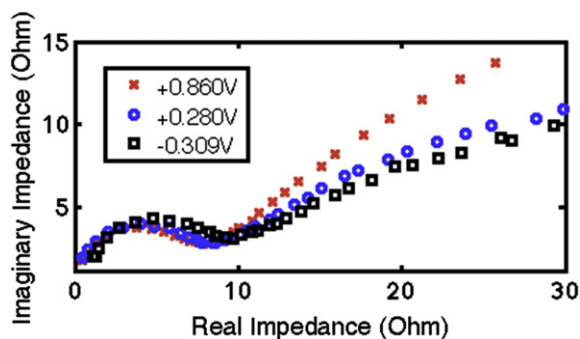


Fig. 6. EIS spectra for the experimental cell at an operational temperature of 900 °C. A portion of the spectra are cut-off in order to show high-frequency detail.

By fitting a transfer function based on this equivalent circuit to the EIS spectral data, extrapolations of the plots can be made and the values of all resistive elements found. The Butler-Volmer model (Equation (18)) of the electrode reaction process can be used to fit the measured activation losses at each electrode as a function of cell current density. The average cell current  $i$  was recorded during each impedance test, and this value of  $i$ , combined with the  $R$  values extracted through the equivalent circuit fit, was used to find the activation overvoltage for each test point through the relation  $\eta = iR$ . By substituting this expression into Equation (16), a relation with only two unknown parameters,  $i_0$  and  $\alpha$ , is produced. This relation was fit to the experimentally derived data points in the  $i$ – $\eta$  plane for each cell temperature, yielding a single value of  $\alpha$  and a temperature dependent value of  $i_0$  for each electrode process.

Since it is desirable to produce a more general model for electrode kinetics as a function of temperature, an Arrhenius Equation is used to model the dependence of the exchange current density  $i_0$  on temperature  $T$ . The Arrhenius equation takes the form

$$i_0 = Ae^{\frac{-E_a}{RT}}, \quad (26)$$

This formulation has the advantage that the exchange current density can be predicted based upon the system temperature  $T$ , and the activation energy  $E_a$  is a general term describing the rate limiting reaction step at the electrode for a given reaction and electrode material pair. Because changes in electrode microstructure will have a limited effect on the chemical pathways in the overall reaction, the activation energy will not have an appreciable dependence upon electrode tortuosity, porosity, or other microstructural parameters. The effect of these parameters on the exchange current density is included through the pre-exponential term  $A$ . This allows the activation energy term to be compared across cells, materials, and devices.

Because it is impossible to discern from EIS fits of a single cell which R/C block corresponds to the anode and which corresponds to the cathode process, the derived activation energies for each electrode were compared against published values in order to identify them.

The results of this analysis are shown below in Fig. 8, and the corresponding Arrhenius terms and the Butler-Volmer dimensionless charge transfer coefficient  $\alpha$  for each electrode are listed in

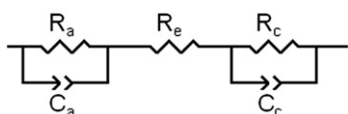


Fig. 7. Equivalent circuit model used to examine the EIS spectra.

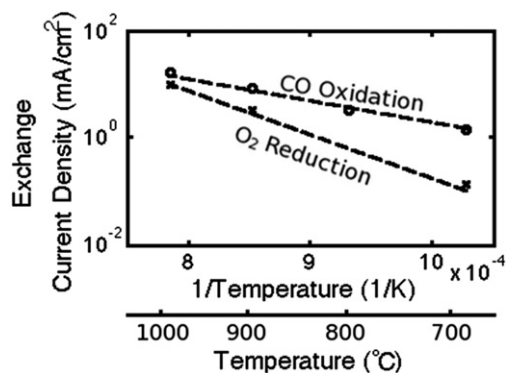


Fig. 8. Arrhenius plots of measured electrode reactions.

Table 3. The activation enthalpy for oxygen reduction on the YSZ-LSM system has been reported in the range of 144–153 kJ mol<sup>−1</sup> [38] in one study and as high as 172 kJ mol<sup>−1</sup> in another [39], within the range found in these experiments. Reliable published results for the activation energy of carbon monoxide oxidation on a Ni-YSZ anode are limited and scattered. One report on CO kinetics on Ni/YSZ bounds the overall activation enthalpy between 41 kJ mol<sup>−1</sup> and 158.1 kJ mol<sup>−1</sup> based upon the energies for some of the elementary reaction steps measured by the authors, although the rate limiting step was not determined [40]. Other studies have calculated values ranging from 59.8 kJ mol<sup>−1</sup> [41] to 136 kJ mol<sup>−1</sup> [42] and even as high as 165 kJ mol<sup>−1</sup> [23]. The values found in this study fall within this expected range.

The model was exercised using these experimentally derived parameters for the conditions tested on the experimental devices. Predicted  $I$ – $V$  responses matched well with the experimental data and the maximum relative error was calculated at 8%. Fig. 9 shows the measured  $I$ – $V$  response at 900 °C, along with the predicted  $I$ – $V$  curve from the model itself.

## 6. Model results and discussion

To better understand the interactions between carbon bed depth, electricity production, and cell efficiency, the model was run with  $r_0$  equal to 1.05 cm, the anode chamber dimension of the experimental button cell device. It should be noted, however, that the choice of  $r_0$  will not affect the model results, as the cell chemical concentration and pressure profiles are constant in the radial direction, and are therefore valid for any planar geometry. An isothermal assumption was used for the model and the temperature was set to 900 °C.

The model was exercised by varying the bed height, and a full current–voltage ( $I$ – $V$ ) curve from cell OCV to the short circuit condition was calculated for each scenario. The cell electrical power that is produced is readily calculated by multiplying the current and voltage together. The overall cell efficiency, Equation (25), was also calculated for each test case. The results of this study are shown in Fig. 10.

The results indicate that the cell configuration studied is capable of supported power densities in excess of 220 mW cm<sup>−2</sup>. As the fuel

Table 3  
Arrhenius parameters of electrode reactions.

	Pre-exponential ( $A$ )	Activation energy ( $E_a$ ) [kJ mol <sup>−1</sup> ]	Charge coefficient ( $\alpha$ )
O <sub>2</sub> Reduction	$2.93 \times 10^4$	$158 \pm 19$	0.40
CO Oxidation	$2.22 \times 10^1$	$78 \pm 9$	0.48

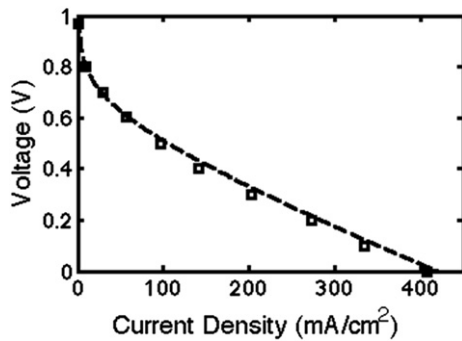


Fig. 9. Predicted  $I$ – $V$  curve overlaid on experimental data.

bed height for the cell is increased, the maximum power density also increases. This trend, however, exhibits strong diminishing returns, and above a bed height of approximately 1 cm, large increases to the bed height result in only minor improvements in the overall maximum cell power density.

The results also show that the cell is able to operate in a regime with greater than 70% overall cell efficiency. As expected, increases in bed height serve to lower the overall cell efficiency, as the carbon dioxide created at the cell anode surface has more residence time in the bed before leaving, and therefore a higher probability of reacting with the fuel and forming carbon monoxide, lowering efficiency.

The results further indicate that a tradeoff exists between maximizing cell efficiency and maximizing cell power density. Along the maximum power line, cell efficiency is in the 25–35% range. Reaching significantly higher efficiencies, on the order of 60%, requires that the cell be operated in a regime that is a factor of two or more below the maximum power density asymptote. For the cell configuration studied, a region exists around a fuel bed height of 5 mm and a cell power density of  $100 \text{ mW cm}^{-2}$ , which results in a cell efficiency of near 60% and balances high power output with high efficiency. Further improvements to both the cell maximum power density and cell efficiency that can enlarge and improve this operating zone are possible with different cell geometries and flow patterns, particularly designs that incorporate a freeboard region with active cell area to scavenge excess CO from the cell exhaust. The general trend, however, will hold for all cells. Holding a cell at the maximum power density point will result in poor cell efficiencies for most bed heights. To maximize efficiency a short bed height should be utilized and a power density below the maximum achievable power density should be chosen.

These results demonstrate that the fuel cell configuration is extremely important, as changes in geometry impact the residence

time that product  $\text{CO}_2$  has in the fuel bed as it makes its way toward the exhaust stream. By correctly designing the cell geometry, this residence time can be controlled so that a majority of the  $\text{CO}_2$  passes through the bed before having a chance to react, while enough does react to continue to provide the necessary CO fuel to the anode surface. This essentially allows the designer to operate the cell in a domain that has excess O (provided through the fuel cell). In other words, in this regime oxygen enters the system faster than the Boudouard reaction can restore thermodynamic equilibrium. This implies that a careful control of geometry to control bed kinetics so that the resultant exhaust gas flow has not had a chance to fully equilibrate through the Boudouard reaction will result in a more efficient cell, albeit one with less CO formation and therefore less power density. This tradeoff in power and efficiency is therefore a tunable parameter, controlled by operation and geometry.

To ensure that the use of experimentally derived exchange current density parameters does not adversely affect the overall efficiencies that are possible in a CFC system, further model runs were conducted in order to test the sensitivity of the results to these parameters. The results indicate that geometries can still be found that generate high overall efficiencies in excess of 70%, but that overall cell power density is impacted by the electrode kinetics. These results demonstrate that the CFC system is capable of oxidizing solid fuel and producing electricity at very high efficiencies, and that further improvements to cell electrodes and components will result in higher power densities, lowering the overall cost of a practical CFC device.

## 7. Conclusion

The results shown in this modeling study demonstrate that a carbon fuel cell has the promise to deliver practical electric power densities from solid carbonaceous fuel sources at high overall cell efficiency. The model was validated against measured results in our lab on a button cell arrangement, and further exercised to predict operational performance for a cell with multiple fuel bed depths. The model predicts an operational point resulting in a cell efficiency of near 60% and an overall cell power density of  $100 \text{ mW cm}^{-2}$ , which represents a balance between maximizing efficiency and power output. Further, the model demonstrates that a tradeoff exists between cell efficiency and power density for carbon fuel cells. Maximizing the overall cell efficiency will require operation at a condition below the peak power density. Conversely, maximizing power density will result in poor overall cell efficiency. These trends mirror behaviors present in other fuel cell technologies. Cell operators will have to choose a set of operating conditions that balance the needs for high efficiency with high power density.

## Acknowledgments

The authors would like to acknowledge the support of the Department of Defense (DOE) National Defense Science and Engineering Graduate (NDSEG) Fellowship (B. R. Alexander).

## Table of symbols

$A$	Arrhenius pre-exponential
$C_k$	molar concentration of species $k$
$D$	gas diffusion coefficient
$D_{\text{eff}}$	effective diffusivity
$E$	voltage
$E_a$	activation energy
$F$	Faraday's constant
$\Delta_f \hat{G}_k$	Gibbs free energy of formation for species $k$

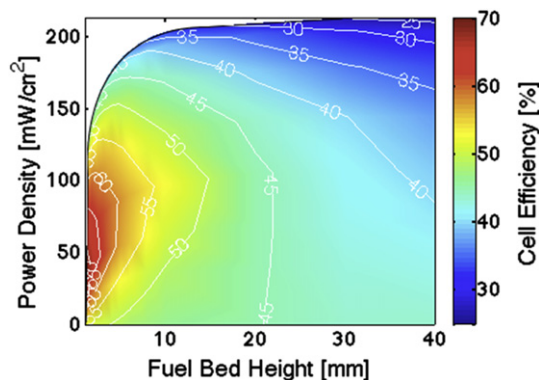


Fig. 10. Model results for a carbon fuel cell device. Overall cell efficiency is plotted as a function of fuel bed height and cell power density. The maximum power density is plotted as a solid line.



$HHV_k$	higher heating value of species k
$i$	current density
$i_o$	exchange current density
$J_k$	flux of species k
$K_p$	equilibrium constant
$m_k$	mass of species k
$\hat{M}_k$	molecular weight of species k
$\eta_{cell}$	cell efficiency
$p$	system pressure
$P_{in/out}$	electric power in/out of cell
$P_o$	standard pressure
$R$	universal gas constant
$\hat{R}_k$	mole-based reaction rate of species k
$S_{g,C}$	specific surface area, char
$T$	system temperature
$t_e$	thickness of the electrolyte layer
$V_{free}$	gas volume in bed
$x_c$	char extent of conversion
$x_k$	molar concentrations of species k
$Y_{c,char}$	mass fraction of carbon in the fuel char
$\alpha$	charge transfer coefficient
$\kappa$	effective bed permeability
$\mu$	viscosity
$\rho$	gas phase density
$\sigma$	conductivity
$\psi$	structural parameter

## References

- [1] A. Demirbas, *Biofuels: Securing the Planet's Future Energy Needs*, Springer, London, 2009.
- [2] Andrew C. Lee, Reginald E. Mitchell, Turgut M. Gür, *AIChE J.* 55 (4) (2009) 983.
- [3] Andrew C. Lee, Siwen Li, Reginald E. Mitchell, Turgut M. Gür, *Electrochem. Solid State Lett.* 11 (2) (2008) B20.
- [4] Siwen Li, Andrew C. Lee, Reginald E. Mitchell, Turgut M. Gür, *Solid State Ionics* 179 (2008) 1549.
- [5] Turgut M. Gür, Michael Homel, Anil V. Virkar, *J. Power Sources* 195 (2010) 1085.
- [6] B.R. Alexander, R.E. Mitchell, T.M. Gür, *J. Electrochem. Soc.* 159 (3) (2012) B347.
- [7] B.R. Alexander, R.E. Mitchell, T.M. Gür, *J. Electrochem. Soc.* 158 (5) (2011) B505.
- [8] K.R. Williams, in: *An Introduction to Fuel Cells*, Elsevier Publishing Company, Amsterdam, 1966 (Chapter 1).
- [9] W.W. Jacques, *Harper's Mag.* 94 (Dec.1896-May 1897) 144.
- [10] F. Haber, L. Bruner, *Z. Elektrochem.* 10 (1904) 697.
- [11] E. Baur, *Z. Elektrochem.* 16 (1910) 300.
- [12] E. Baur, H. Ehrenberg, *Z. Elektrochem.* 18 (1912) 1002.
- [13] E. Baur, H. Preis, *Z. Elektrochem.* 43 (1937) 727.
- [14] D.H. Archer, R.L. Zahradnik, *Chem. Eng. Progr. Symp. Ser.* 63 (1967) 55.
- [15] R.D. Weaver, S.C. Leach, A.E. Bayce, L. Nanis, *Direct Electrochemical Generation of Electricity from Coal* 94025; SAN-0115/105–1, SRI, Menlo Park, CA, 1979.
- [16] N.J. Cherepy, R. Krueger, K.J. Fiet, A.J. Jankowski, J.F. Cooper, *J. Electrochem. Soc.* 152 (1) (2005) A80.
- [17] T. Tao, *Liquid Anode Fuel Cell for Direct Carbon Conversion*, Presented at Direct Carbon Conversion Workshop, FuelCell Seminar, Palm Springs, November 14, 2005.
- [18] T. Tao, *Carbon–Oxygen Fuel Cell*, US Patent 6,692,861 B2, February 17, 2004.
- [19] S. Gopalan, G. Ye, U.B. Pal, *J. Power Sources* 162 (2006) 74.
- [20] V. Yentekakis, P.G. Debenedetti, B. Costa, *Ind. Eng. Chem. Res.* 28 (1989) 1414.
- [21] S. Zecevic, E.M. Patton, P. Parhami, 1983, *Carbon* 42 (2004).
- [22] D. Cao, Y. Sun, G. Wang, *J. Power Sources* 167 (2007) 250.
- [23] S. Giddey, S. Badwal, A. Kulkarni, C. Munnings, *Prog. Energy Combust. Sci.* 38 (2012) 360.
- [24] T.M. Gür, R.A. Huggins, *J. Electrochem. Soc.* L95 (1992).
- [25] Qinghua Liu, Ye Tian, Chun Xia, Levi T. Thompson, Bin Liang, Yongdan Li, *J. Power Sources* 185 (2008) 1022–1029.
- [26] Yixiang Shi, Chen Li, Ningsheng Cai, *J. Power Sources* 196 (2011) 5526–5537.
- [27] C. Ozgur Colpan, Ibrahim Dincer, Feridun Hamdullahpur, *Int. J. Hydrog. Energy* 32 (2007) 787–795.
- [28] T.M. Gür, *J. Electrochem. Soc.* 157 (5) (2010) B571.
- [29] T. Horita, N. Sakai, T. Kawada, H. Yokokawa, M. Dokiya, *J. Electrochem. Soc.* 142 (8) (1995) 2621.
- [30] N. Nakagawa, M. Ishida, *Ind. Eng. Chem. Res.* 27 (1988) 1181.
- [31] S. Nürnberger, R. Bussar, P. Desclaux, B. Franke, M. Rzepka, U. Stimming, *Energy Environ. Sci.* 3 (2010) 150.
- [32] Y. Wu, C. Su, C. Zhang, R. Ran, Z.Z. Shao, *Electrochem. Commun.* 11 (2009) 1265.
- [33] L. Ma, *Combustion and Gasification of Chars in Oxygen and Carbon Dioxide at Elevated Pressure*, Dissertation, Stanford, CA, Mechanical Engineering Dept., Stanford University, 2006.
- [34] E. Teller, S. Brunauer, P.H. Emmett, *J. Am. Chem. Soc.* 60 (1938) 309–319.
- [35] R.R. Rounsley, *J. AIChE* 7 (2) (1961) 308–311.
- [36] S.K. Bhatia, D.D. Perlmutter, *AIChE J.* 26 (1980) 379–386.
- [37] R.B. Bird, W.E. Stewart, E.N. Lightfoot, *Transport Phenomena*, Wiley, New York, 1960.
- [38] E.P. Murray, T. Tsai, S.A. Barnett, *Solid State Ionics* 110 (1998) 235.
- [39] V. Yurkiv, D. Starukhin, H.-R. Volpp, W.G. Bessler, *J. Electrochem. Soc.* 158 (1) (2011) B5–B10.
- [40] O.A. Marina, L.R. Pederson, M.C. Williams, G.W. Coffey, K.D. Meinhardt, C.D. Nguyen, E.C. Thomsen, *J. Electrochem. Soc.* 154 (5) (2007) B452–B459.
- [41] A. Mary Sureshini, Bahman Habibzadeh, Benjamin P. Becker, Chad A. Stoltz, Bryan W. Eichhorn, Gregory S. Jackson, *J. Electrochem. Soc.* 153 (4) (2006) A705–A715.
- [42] A. Utz, A. Leonide, A. Weber, E. Ivers-Tiffée, *J. Power Sources* 196 (2011) 7217–7224.